Materials Advances

ROYAL SOCIETY OF CHEMISTRY

PAPER

View Article Online
View Journal | View Issue

Cite this: *Mater. Adv.*, 2023, 4, 3061

Molecular engineered A–D–A–D–A organic electrode system for efficient supercapacitor applications†

Sudhir D. Jagdale,[ac] Chepuri R. K. Rao,*[ac] Sidhanath V. Bhosale *[ac] and Sheshanath V. Bhosale *[b]

Pseudocapacitors (PSCs) play a key role in energy storage (ES) technology development today. PSCs offer higher energy density as compared to their inorganic counterparts. Moreover, as compared to battery systems, they also exhibit higher power density for a shorter duration of time. In the present investigation, we designed, synthesized and demonstrated a novel acceptor (A)–donor (D)–acceptor (A)–donor (D)–acceptor (A) molecular architecture comprising naphthalene-1,4,5,8-tetracarboxylic diimide (NDI), tryptophan (Trp) and dopamine (**DP**) organic components. The as-fabricated **NDI-Trp-DP**/graphite foil (GF) electrode material was employed for three-electrode supercapacitor (SC) and two-electrode symmetric supercapacitor (SSC) device fabrication. The **NDI-Trp-DP**/GF material exhibited pseudocapacitive behaviour with an excellent specific capacitance (C_{sp}) of about 267.90 F g^{-1} at a scan rate of 5 mV s^{-1} (cyclic voltammetry, CV) and 323 F g^{-1} at a current density 0.5 A g^{-1} (galvanostatic charge–discharge, GCD) in a three-electrode SC and a C_{sp} of 152 F g^{-1} at 0.5 A g^{-1} in two-electrode SSC device systems. The **NDI-Trp-DP**/GF electrode exhibits an excellent cycling stability of about 95.87% after 10 000 galvanostatic charging–discharging (GCD) cycles and 97.76% continuous GCD charge–discharge cycling coulombic efficiency. The enhanced C_{sp} and cycling stability performance of the **NDI-Trp-DP**/GF electrode results from the reversible redox reactions of the organic subunits present in the molecule, faster ion diffusion, and improved mechanical and chemical stability. This novel A–D–A–D–A design offers an efficient way to improve the electrochemical performance of PSCs. The design of this molecular engineered architecture and its redox properties with excellent cycling stability will help to fabricate future PSC-based electronics.

Received 13th June 2023,
Accepted 26th June 2023

DOI: 10.1039/d3ma00296a

rsc.li/materials-advances

Introduction

The growing energy demand depends significantly on fossil fuels. The excessive utilization of natural resources is exerting ever-increasing pressure on the environment, causing climate change and forest fires. Therefore, to meet our energy demands, alternative energy resources such as sunlight, geothermal heat, seawater and wind are utilized.[1] Energy harvesting from these renewable resources and their storage utilizing greener technologies are currently demanded.[2] To provide more reliable, sustainable and environmentally friendly technologies with high energy and high power, research and development efforts towards small-scale energy storage (ES) devices, *i.e.*, batteries and supercapacitors (SCs), are required.[3] Batteries and SCs are utilized in hybrid electric vehicles, electronic devices such as mobiles, wearable electronics and flexible displays.[4,5] Although rechargeable batteries exhibit higher energy density, they provide lower power density due to their slow charging–discharging rate and suffer from poor cycling stability.[6,7] SCs have attracted the attention of researchers as ES devices because of their high power density, longer cycle life and fast charging–discharging rate.[8,9] Therefore, SCs have the potential to meet the increasing energy demand of modern society. However, SCs exhibit some limitations, *i.e.*, lower energy density than batteries, which in turn result in limited practical applications, especially in portable electric devices. Therefore, researchers have focused on the development of SCs with higher energy density, higher power density and ultra-long electrochemical stability. Such SC devices are essential for the development of cutting-edge technology products.[10] SCs are

[a] *Polymers and Functional Materials Division, CSIR-Indian Institute of Chemical Technology, Hyderabad-500007, Telangana, India. E-mail: ramchepuri@iict.res.in, bhosale@iict.res.in*
[b] *Department of Chemistry, School of Chemical Sciences, Central University of Karnataka, Kadaganchi, Kalaburagi-585 367, Karnataka, India. E-mail: bsheshanath@gmail.com*
[c] *Academy of Scientific and Innovative Research (AcSIR), Ghaziabad-201002, Uttar Pradesh, India*

† Electronic supplementary information (ESI) available. See DOI: https://doi.org/10.1039/d3ma00296a

classified into two major categories: (i) electric double-layer capacitors (EDLCs) and (ii) pseudocapacitors based on the electrochemical energy storage mechanism.[11] EDLCs store energy through the adsorption/desorption mechanism at the interface between the electrode and electrolyte materials on the double layer. EDLCs exhibit very limited energy density and low electrochemical capacity.[12] In comparison, pseudocapacitors displayed greater energy storage on the electrode surface through rapid reversible faradaic redox reactions.[8,13] Therefore, PSCs are fabricated with high-energy-density electrodes, which can boost the specific capacitance (C_{sp}).

Graphene-based materials have been utilized for fabrication of EDLCs as well as PSCs. Herein, the functional groups of graphene-based materials are involved in reversible redox reactions, exhibiting pseudocapacitive properties.[14] However, graphene-, CNT- and reduced-graphene-oxide-based materials are insufficient to achieve a high C_{sp}.[15] Therefore, pseudocapacitor materials include transition metal oxides,[16] precious metal oxides, *e.g.*, RuO_2[17] and IrO_2,[18] and conducting polymers, *i.e.*, polyaniline[19] and polypyrrole.[20] However, metal oxides and conducting polymers exhibited poor stability and low electrical conductivity.[21] To overcome all these limitations, it is important to develop appropriate electrode materials with suitable redox subunits for improving the electrochemical performance of the next-generation low-cost PSCs. Electrode materials based on organic compounds are an attractive green alternative for the fabrication of PSCs.[22–25] It is notable that organic electrode materials have underperformed compared with inorganic materials.[26] To incorporate the desired physical, chemical and electrochemical properties: (i) higher power density, (ii) energy density, and (iii) rate capability, and (iv) longer cycle life, the design and synthesis of novel organic molecules are required. These properties can be achieved by incorporating multiple electronic reversible redox-active subunits in the organic molecular architecture.[27–29] To achieve the highest C_{sp} with a long cycle life and stability, the fabrication of PSCs based on organic electrode materials, both electron-accepting and electron-donating subunits in the molecular framework with a wide potential range are required.[30] In addition, fast surface reactions can be enhanced by utilizing a π-conjugated molecular skeleton.[31]

Herein, we develop a **NDI-Trp-DP** (naphthalenediimide-tryptophan-dopamine) molecular architecture fabricated from the π-conjugated symmetric naphthalene-1,4,5,8-tetracarboxylic diimide (NDI), the amino acid tryptophan (Trp) and the neurotransmitter dopamine (**DP**). These subunits were selected based on their electron donor (D) and electron acceptor (A) properties. Generally, such A–D–A–D–A molecular architectures provide substantial delocalization of the π-electrons over the system, which in turn enhances the polarizability and energy-gap manipulation between the highest occupied molecular orbital (HOMO) and lowest unoccupied molecular orbital (LUMO). Redox-active-molecular-scaffold-, donor–acceptor-based organic electrode systems have not been fully explored for energy storage applications.[32] Such materials are more appealing, as one can tune the donor and acceptor redox properties by manipulating the chemical structure design for utilization in SCs.[32] The donor and acceptor subunits in the molecular architecture could enhance the intramolecular charge transfer between the donor and acceptor, which in turn would lead to an enhancement in the operating voltage. Herein, the electron transfer between the organic electrode material and electrolyte can increase the performance of the SCs. NDIs are employed in various optoelectronic applications due to their electrochemical and optical properties and molecular stability.[33] Moreover, NDI-based organic electrode materials have been utilized for energy storage applications.[29,34,35] Tryptophan (Trp), an aromatic amino acid, is the most electron-rich π-system bearing an indole subunit, which can exhibit electron-donating properties.[36,37] A redox-active tryptophan-based graphene quantum dot hybrid material was employed in supercapacitor applications.[38] A tryptophan–picric acid complex was utilized for SC applications by Srinivasan *et al.*[39] Very recently, Zaijun and co-workers employed RuO_2-functionalized graphene quantum dots for flexible supercapacitor applications.[40] Dopamine (**DP**) is a naturally occurring neurotransmitter molecule that plays an important role in the body.[41] Recent studies have shown that **DP** can be efficiently utilized in energy storage applications.[34b,42–46] Thus, in the design of **NDI-Trp-DP**, we considered three major principles: (i) A–D–A–D–A molecular architecture; (ii) the selection of multiple redox systems, which may enhance the potential window; and (iii) an aromatic π-conjugated surface involved in pseudocapacitive behaviour to increase the surface redox reactions on the organic molecular electrode through electrolyte or ion interactions, which in turn will enhance the rate capability. Here, for the first time, we demonstrate the utilization of an A–D–A–D–A molecular architecture as a redox-active organic electrode material in a PSC device. We fabricated electrodes comprising **NDI-Trp-DP** on a graphite foil (GF) surface. The as-fabricated electrode **NDI-Trp-DP**/GF electrode material exhibited excellent electrochemical properties with outstanding cycling stability. Real-world applications were demonstrated by constructing symmetric supercapacitor two-electrode systems (SSE) and employed as an energy storage device. The supercapacitor results in an SSE system, demonstrating the potential of the **NDI-Trp-DP** (A–D–A–D–A) systems in SC technologies.

Experimental section

Materials

1,4,5,8-Naphthalenetetracarboxylic dianhydride (**NDA**) (>95.0%) was purchased from TCI (Hyderabad), and tryptophan (≥98%) and dopamine hydrochloride were purchased from Sigma-Aldrich (Hyderabad) Pvt. Ltd, India. *N,N*-Dimethylformamide (DMF) (99.50%), methanol (99.50%), HCl (35–38%), sulphuric acid (H_2SO_4) (95.0–98%) and *N*-methyl-2-pyrrolidone (C_5H_9NO) (99.0%) were purchased from Finar (Ahmadabad/Mumbai), India Limited. Graphite foil (GF) was purchased from Falcon Graphite Industries, India, and carbon black (super p-conductive) (99.0+%) and polytetrafluoroethylene (PTFE) were procured from Alfa Aesar India.

Structural characterizations

^{1}H NMR and ^{13}C NMR spectra were performed using a Bruker Avance-400 MHz spectrometer and 100 MHz spectrometer, respectively. FT-IR spectra were performed using a PerkinElmer Spectrum (Spectrum 100; PerkinElmer) instrument. MALDI-TOF experiments were performed using a Shimadzu Biotech Axima performance spectroscopic instrument. A Thermofisher Exactive Orbitrap instrument was used for HRMS measurements. TGA was performed using a Q-500 TGA under an N_2 atmosphere. At a rate of 10 °C min^{-1}, the samples were heated to 800 °C. The detailed morphology of the synthesized samples of **NDI-Trp-DP** were examined using FE-SEM (Quanta FEG 250).

Electrochemical measurements

The electrochemical experiments (CV, GCD and EIS) were performed using an AUTOLAB (potentiostat and galvanostat, 320N, Netherlands) ZIVE LAB (MP 5) at room temperature. For the three-electrode device, **NDI-Trp-DP**/GF (working), platinum (Pt) wire (counter) and Ag/AgCl(sat. KCl) (reference) electrodes were used in aq. 1 M H_2SO_4 electrolyte. CV was carried out at different scan rates, *i.e.*, 5, 10, 15, 20, 25, 30, and 35 mV s^{-1}, and GCD was carried out at current densities of 0.5, 1, 2, 3, 4, 5, and 10 A g^{-1}. EIS was measured at frequencies of 0.01 Hz to 100 kHz at 0 V bias conditions with a 10 mV AC sinus perturbation.

Synthesis of (2*S*,2′*S*)-2,2′-(1,3,6,8-tetraoxo-1,3,6,8-tetrahydrobenzo-[*lmn*] [3,8] phenanthroline-2,7-diyl)bis(3-(1-hydroxyindol-3-yl)propanoicacid) (NDI-Trp)[47]

1,4,5,8-Naphthalenetetracarboxylicdianhydride (1 g, 3.70 mmol) and L-tryptophan (1.52 g, 7.40 mmol) were suspended in 10 mL of dimethylformamide (DMF) in a 100 mL round bottom flask under an N_2 atmosphere and stirred for 10 min at room temperature. Triethylamine (TEA) (0.5 mL) was then added. The reaction mixture was refluxed for 12 h. The completion of the reaction was monitored using TLC. The mixture was cooled to room temperature. Under reduced pressure, the DMF was removed. 200 mL of 2 N HCl was added with stirring for 1 h. The reaction mixture was filtered and washed three times with distilled water, and then dried under high vacuum at 100 °C to yield **NDI-Trp** (80%). FT-IR (γ, cm^{-1}, KBr) 3410, 2934, 1710, 1640, 1343, 742; ^{1}H NMR (400 MHz, DMSO-d$_6$) δ ppm: 10.66 (2H, s), 8.60 (4H, s), 7.47 (2H, d, J = 7.9 Hz), 7.20 (2H, d, J = 8.1 Hz), 7.05 (2H, d, J = 2.3 Hz), 6.94 (2H, t, J = 7.5 Hz), 6.81 (2H, t, J = 7.9 Hz), 5.85 (2H, dd, J = 9.1, 5.5 Hz), 3.69 (2H, dd, J = 15, 5.3 Hz), 3.50 (2H, dd, J = 14.9, 9.2 Hz); ^{13}C NMR (100 MHz, DMSO-d$_6$): 171.0, 162.5, 136.3, 131.6, 127.5, 126.4, 126.1, 124.1, 121.2,118.7, 118.4, 11.7, 110.6, 54.8, 24.5; ESI-MS (*m*/*z*): 640.16 [M]$^+$; HRMS: calcd for $C_{36}H_{25}O_8N_4$ (M + H)$^+$: 641.1666, found 641.1695 (M + H)$^+$; MALDI-TOF $C_{36}H_{24}O_8N_4$ = 640.16 [M]$^+$, found 663.178 [M + Na]$^+$.

Synthesis of (2*S*,2′*S*)-2,2′-(1,3,6,8-tetraoxo-1,3,6,8-tetrahydrobenzo-[*lmn*][3,8]phenanthroline-2,7-diyl)bis(*N*-(3,4-dihydroxyphenethyl)-3-(1-hydroxyindol-3-yl)propanamide) (NDI-Trp-DP)[48a]

The compound **NDI-Trp** (500 mg, 780.05 mmol), *N*-(3-dimethylaminopropyl)-*N*′-ethylcarbodiimide (EDC) hydrochloride (448 mg, 2340.15 mmol) and 1-hydroxybenzotriazolehydrate (HOBT) (316 mg, 2340.15 mmol) were suspended in 15 mL dimethylformamide (DMF) in a 100 mL round bottom flask under a nitrogen atmosphere. The reaction mixture was then stirred for half an hour at 0 °C. Dopamine (**DP**) (358 mg, 2340.15 mmol) and *N*,*N*-diisopropylethylamine (DIPEA) (0.5 mL) were added to the reaction mixture under a nitrogen atmosphere and stirred for 48 h at room temperature. The completion of the reaction was monitored using TLC. After consumption of the starting material, the reaction mixture was allowed to cool at room temperature. Under reduced pressure, the DMF was removed, and the mixture was then poured into ice-cold water. Under vacuum, the obtained precipitate was filtered and washed with hot water (100 mL) followed by hot methanol (50 mL). The dark brown product (**NDI-Trp-DP**) was dried overnight at 100 °C. Yield: 77%; FT-IR (γ, cm^{-1}, KBr) 3406, 2906, 1705, 1664, 1581, 1452, 1341, 748; ^{1}H NMR (400 MHz, DMSO-d$_6$) δ ppm: 10.57 (2H, s), 8.70 (4H, s), 8.54 (4H, s), 8.08 (2H, s),7.45 (2H, d, J = 7.8 Hz), 7.15 (2H, d, J = 7.9 Hz), 6.97–6.87(4H, m), 6.81 (2H, t, J = 7.4 Hz), 6.65–6.53 (4H, m), 6.41 (2H, d, J = 7.8 Hz), 5.76 (2H, dd, J = 9.4, 5.1 Hz), 3.84–3.65 (2H, m), 3.62–3.43 (4H, m), 3.18 (6H, s). ^{13}C NMR (100 MHz, DMSO-d$_6$): 168.6, 162.8, 145.5, 143.9, 136.3, 130.9, 127.6, 127.0, 126.8, 126.5, 123.9, 121.2, 119.7, 118.7, 118.4, 116.4, 15.9, 111.6, 110.8, 55.7, 41.7, 35.2, 23.9; ESI-MS (*m*/*z*): 911 [M]$^+$; MALDI-TOF $C_{52}H_{43}O_{10}N_6$ = 911.303 [M]$^+$; found 933.391 [M + Na]$^+$; HRMS: calcd for $C_{52}H_{43}O_{10}N_6$ = 911.3035 [M]$^+$, found 911.3067 [M]$^+$.

Cyclic voltammetry (CV)

The CV measurements were carried out utilizing a ZIVE LAB (MP 5) series potentiostat instrument. 0.1 M tetrabutylammonium hexafluorophosphate electrolyte was prepared in dimethylformamide (20 mL). A 3 mm glassy carbon (working) electrode, Ag/AgCl (sat. KCl) electrode[48b,c,d] as a reference and a Pt wire electrode as a counter were utilized. The CV measurements were recorded at a scan rate of 10 mV s^{-1} under a nitrogen atmosphere. 10 mg of **NDI-Trp-DP** was utilized for CV measurements. In the Ag/AgCl (sat KCl) aqueous electrode, we used a Luggin capillary for avoiding water interference.

Electrode fabrications

In order to construct the working electrode, a slurry of **NDI-Trp-DP**, carbon black (super p-conductive) as the conductive material and polytetrafluoroethylene (PTFE) as a binder was used. The three components were mixed thoroughly by grinding in weight ratios of 70 : 20 : 10 (14 : 4 : 2 mg). A homogeneous slurry was prepared by hand grinding using a mortar and pestle with *N*-methyl-2-pyrrolidone (NMP) as a solvent. The as-prepared slurry was precisely coated on a graphite foil (GF) with dimensions of 1 × 1 cm^2. The electrode material was placed in a hot air oven at 80 °C for 12 h. The mass of the organic active material **NDI-Trp-DP** in the electrodes was maintained at nearly 2 mg.

Fabrication of symmetric supercapacitor device (NDI-Trp-DP/GF//NDI-Trp-DP/GF)

The symmetric **NDI-Trp-DP**/GF supercapacitor device was fabricated utilizing a Swagelok cell. The **NDI-Trp-DP**/GF electrodes

were employed as a pair of electrodes, *i.e.*, as the anode and cathode. A piece of filter paper (Whatman) was used as a separator. 1 M H_2SO_4 as an electrolyte was dropped between **NDI-Trp-DP**/GF/separator/**NDI-Trp-DP**/GF interface.

Formulae used:

C_{sp} from the three-electrode CV studies:[49]

$$C_{sp} = \frac{\int I\,dV}{2 \times v \times m \times \Delta V} \quad (1)$$

C_{sp} from the three-electrode GCD investigation:[49]

$$C_{sp} = \frac{I \times \Delta t}{m \times \Delta V} \quad (2)$$

where C_{sp} is the specific capacitance (F g^{-1}), I is the response current (A), v is the potential scan rate (mV s^{-1}), m is the mass of the active material (g), Δt is the discharge time (s), and ΔV is the voltage window (V).

C_{sp} from the two-electrode GCD studies:[49]

$$C_{sp} = 4\left(\frac{I \times \Delta t}{m \times \Delta V}\right) \quad (3)$$

where C_{sp} = the specific capacitance (F g^{-1}), I = the response current (A), v = the potential scan rate (mV s^{-1}), m = the active material average mass of both electrodes (g), Δt = the discharge time (s), and ΔV = the voltage window (V).

Energy density was estimated from the two-electrode GCD studies:[49]

$$E = \frac{1}{8} \times C_{sp}(\Delta V)^2 \quad (4)$$

Power density was evaluated from the two-electrode GCD analysis:[49]

$$P = \frac{E}{\Delta t} \quad (5)$$

Where C_{sp} = the specific capacitance (F g^{-1}), ΔV = the voltage window (V), E = the energy density (W h kg^{-1}), and P = the power density (W kg^{-1}).

The coulombic efficiency of **NDI-Trp-DP**/GF//**NDI-Trp-DP**/GF device was analyzed using the equation[50]

$$\mathrm{nc} = \frac{\mathrm{td}}{\mathrm{tc}} \times 100\% \quad (6)$$

where td and tc denote the discharge time and charge time of the symmetric supercapacitor device.

Results and discussion

Synthesis and characterization of NDI-Trp-DP

The synthesis of **NDI-Trp-DP** is represented in Scheme 1. **NDI-Trp-DP** was synthesized by adopting a multistep synthetic reaction strategy following a previously reported procedure.[47,48] **NDI-Trp** was obtained by reacting naphthalene dianhydride (**NDA**) with tryptophan (Trp) in DMF at 100 °C for 24 h based on a procedure reported in the literature.[47] **NDI-Trp** was further reacted with dopamine (**DP**) *via* an amide coupling reaction in the presence of EDC, HOBT and DIPEA in DMF for 48 h at room temperature to yield **NDI-Trp-DP** (Fig. 1a).[48]

FT-IR, ^{1}H and ^{13}C NMR spectroscopy and HRMS spectrometry techniques were used to establish the chemical structure of **NDI-Trp** and **NDI-Trp-DP** (Fig. S1 to S10, ESI†). Thermogravimetric analysis (TGA) in a nitrogen atmosphere revealed that **NDI-Trp-DP** is thermally stable, showing 5% weight loss at about 300 °C (Fig. 1b). Field-emission scanning electron microscopy (FE-SEM) revealed that **NDI-Trp-DP** exhibited a 2D-sheet-like morphology (Fig. 1c). The cyclic voltammogram (CV) of **NDI-Trp-DP** in DMF/0.1 M tetrabutylammonium hexafluorophosphate was recorded in the −1.6 to 1.6 V potential window at a scan rate of 10 mV s^{-1} and exhibited two reversible redox peaks (Fig. 1d). Two reduction peaks of **NDI-Trp-DP** appeared at −0.58 and −1.03 V and were attributed to the NDI subunits,[33] and two oxidation peaks were found at +0.55 and +1.07 V. These oxidation peaks are typical for Trp.[51] The CV curve was utilized to calculate the onset oxidation (0.30 V) and reduction onset (−0.48 V) potential (*vs.* Ag/Ag^+) of **NDI-Trp-DP**. The highest occupied molecular orbital (HOMO) and lowest unoccupied molecular orbital (LUMO) were evaluated to be 4.70 eV and

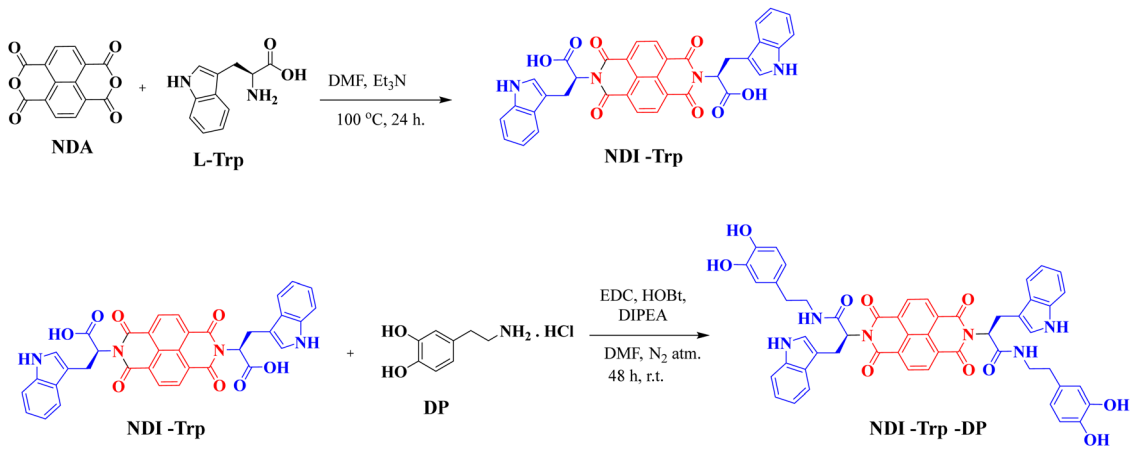

Scheme 1 Synthesis of **NDI-Trp-DP**.

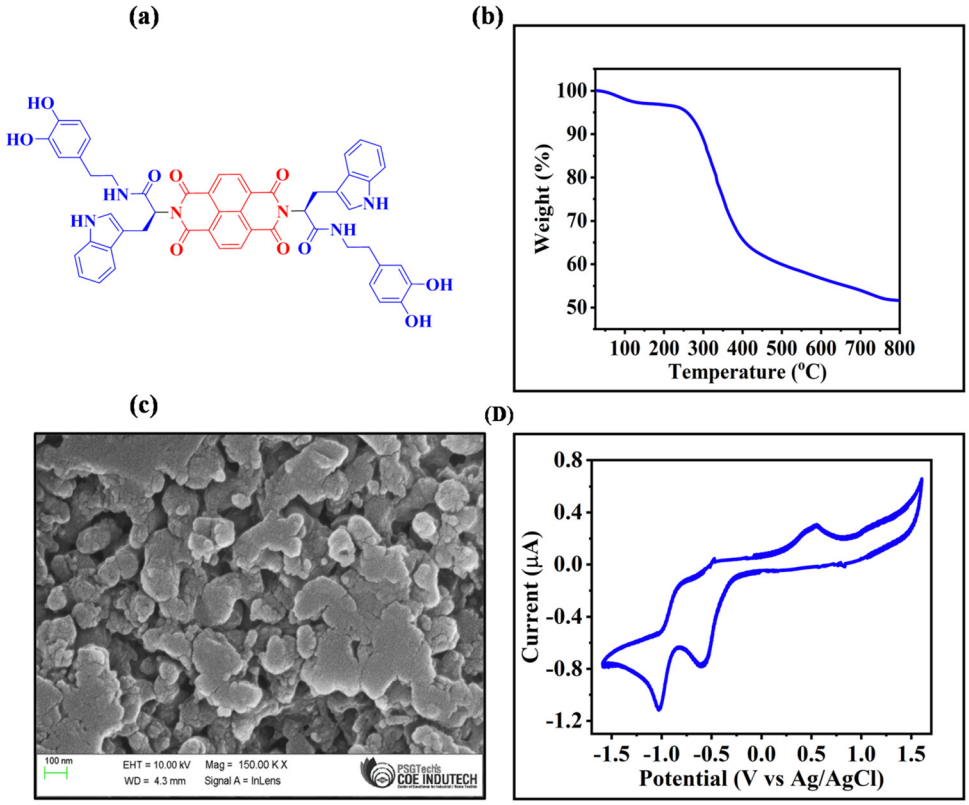

Fig. 1 (a) Molecular structure of naphthalene diimide bolaamphiphile **NDI-Trp-DP**. (b) TGA profile curve of **NDI-Trp-DP**. (c) SEM image of **NDI-Trp-DP**. (d) CV of **NDI-Trp-DP** in dimethylformamide with 0.1 M tetrabutylammonium hexafluorophosphate as an electrolyte.

3.92 eV from E_{onset}^{ox} and E_{onset}^{red} using the formulas HOMO = −e [E_{onset}^{ox} + 4.4] eV and LUMO = −e [E_{onset}^{red} + 4.4 eV], respectively. From the HOMO and LUMO energy levels, the calculated energy gap was found to be 0.78 eV, indicating that the **NDI-Trp-DP** material can be adopted for electrochemical energy storage applications.

Three-electrode system

The as-prepared **NDI-Trp-DP**/GF was utilized as an electrode material for SC applications. The electrochemical properties of GF and **NDI-Trp-DP**/GF were studied using CV measurements in 1 M H_2SO_4 within the potential window of 0 to 1.0 V at 5 mV s^{-1} in the three-electrode system. The CV measurement results of GF and **NDI-Trp-DP**/GF are depicted in Fig. 2a. At 5 mV s^{-1}, the CV curve of GF *vs.* Ag/AgCl exhibited a pair of strong redox peaks at 0.35 V (anodic) and 0.39 V (cathodic), which were ascribed to the faradaic reversible redox reactions. Thus, the CV curve shape of GF displays the pseudocapacitive behavior of the electrode and is totally different than that of the double-layer energy storage mechanism.[52] In comparison, the CV curve of **NDI-Trp-DP**/GF displays a pair of well-resolved reversible redox peaks at about 0.43 V and 0.52 V, which were ascribed to the pseudocapacitive characteristics of the electrode material.[53] These redox peaks are attributed to the oxidation and reduction of **NDI-Trp-DP** active subunits on the electrode surface. The faradaic reversible peaks are symmetric in nature, suggesting that the electrode material comprising **NDI-Trp-DP**/GF could exhibit outstanding electrochemical properties through pseudocapacitive behaviour.[54] Fig. 2b exhibits the CV measurement curves of the three-electrode SC device at scan rates of 5, 10, 15, 20, 25, 30 and 35 mV s^{-1} within the potential window of 0 to 1.0 V. The shapes of all the CV curves suggest pseudocapacitive characteristics. The C_{sp} calculated from CV curve of **NDI-Trp-DP**/GF at 5 mV s^{-1} using eqn (1) (Experimental Section) was found to be 267.90 F g^{-1} (Fig. 2b and Table 1). As the scan rate increased from 5 to 35 mV s^{-1}, the peak intensity of CV curve rapidly increased with small changes in the cathodic peak to the right and anodic peak to the left. The shifting of the cathodic and anodic peak towards more positive and negative values was ascribed to an enhancement of the internal diffusive resistance with increasing scan rate in pseudocapacitive materials.[55] From Fig. 2b, we observed that the CV curve at a higher scan rate of about 35 mV s^{-1} retains its shape, indicating the capacitive behaviour of the **NDI-Trp-DP**. Moreover, as we moved from a lower scan rate of 5 mV s^{-1} to a higher one of 35 mV s^{-1}, the estimated C_{sp} was found to be 104.33 F g^{-1}. The gradual decrease in C_{sp} was ascribed to the slow redox reaction at high scan rate. At a scan rate of 35 mV s^{-1}, **NDI-Trp-DP**/GF displays 35% specific capacitance retention, suggesting the feasibility of the **NDI-Trp-DP**/GF electrode material in supercapacitor applications (Table 1 and Fig. S11a, ESI†). GCD experiments were performed to examine the electrochemical properties of **NDI-Trp-DP**/GF in the three-electrode SC system. The GCD profiles of the GF (red curve) and **NDI-Trp-DP**/GF (black curve) electrodes in the potential window 0

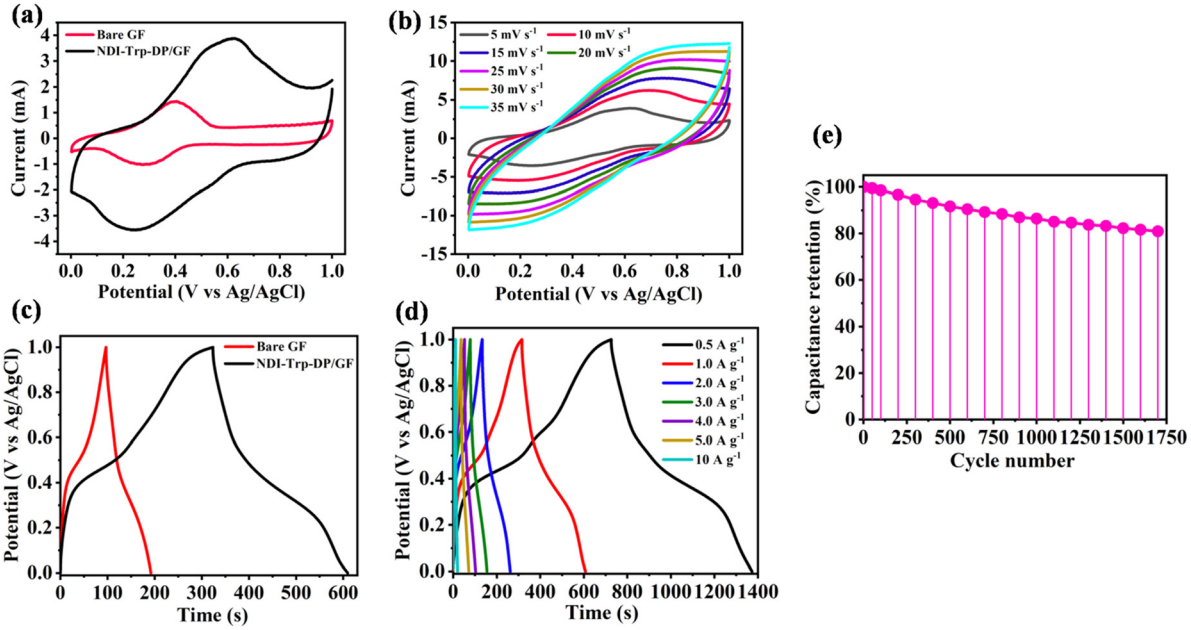

Fig. 2 (a) Comparison of the CVs of bare GF and **NDI-Trp-DP**/GF at a 5 mV s^{-1} scan rate. (b) CVs of the **NDI-Trp-DP**/GF three electrode system device at 5, 10, 15, 20, 25, 30, and 35 mV s^{-1}. (c) GCD curves of bare GF and **NDI-Trp-DP**/GF at a current density of 1 A g^{-1}. (d) Three-electrode system **NDI-Trp-DP**/GF GCD profiles at 0.5, 1, 2, 3, 4, 5, and 10 A g^{-1}. (e) Cycling stability from GCD profile calculated at 4 A g^{-1}.

Table 1 C_{sp} from the CV and GCD profiles at various scan rates and current densities (three-electrode system) for **NDI-Trp-DP**/GF

CV analysis		GCD analysis	
Scan rate mV s^{-1}	Specific capacitance (F g^{-1})	Current density (A g^{-1})	Specific capacitance (F g^{-1})
5	267.90	0.5	323
10	211.65	1	292
15	174.60	2	256
20	149.31	3	231
25	134.27	4	203.03
30	114.64	5	177
35	104.33	10	92.80

to 1.0 V *versus* Ag/AgCl at 1 A g^{-1} current density were recorded and are depicted in Fig. 2c. The GCD curve area of **NDI-Trp-DP**/GF is higher than that of GF. Moreover, **NDI-Trp-DP**/GF exhibited an almost symmetrical charging and discharging GCD curve, suggesting that the electrode material had good pseudocapacitive behaviour due to faradaic redox reactions and electrochemical reversibility.[56] The GCD curves recorded for **NDI-Trp-DP**/GF at current densities of 0.5, 1, 2, 3, 4, 5 and 10 A g^{-1} within the 0 to 1.0 V applied potential window at room temperature are presented in Fig. 2d. The C_{sp} calculated using eqn (2) (Experimental Section) from the GCD curve of **NDI-Trp-DP**/GF at 0.5 A g^{-1} current density was 323 F g^{-1} (Fig. 2d and Table 1). The GCD data suggest that the **NDI-Trp-DP**/GF electrode-containing three-electrode SC exhibited the best charge storage capacity. With increasing the current density from 0.5 to 10 A g^{-1}, the estimated C_{sp} value of the **NDI-Trp-DP**/GF electrode decreased to 92.8 F g^{-1} (Fig. 2d and Table 1). At 10 A g^{-1} current density, a C_{sp} retention of 28.48% was found (Table 1 and Fig. S11b, ESI†), indicating the feasibility of the **NDI-Trp-DP**/GF electrode material in SC applications. The cycling stability of the **NDI-Trp-DP**/GF electrode at 4 A g^{-1} over 1700 GCD cycles was examined, and the capacitance retention was found to be 80.95% (Fig. 2e). We performed the three-electrode-system experiments to confirm the reproducibility of the results using CV and GCD, and we found that the results were consistent in the presence of aqueous electrolyte and Ag/AgCl as a reference electrode (Fig. S12, ESI†). Thus, the **NDI-Trp-DP**/GF electrode material was found to be stable enough for long-term cycling performance. From the above three-electrode SC device results, it could be confirmed that increasing the number of redox subunits could improve the electrode conductivity and the exposure of high surface area could allow more active sites in contact with the electrolyte, which in turn enhanced the pseudocapacitive behaviour of the **NDI-Trp-DP**/GF electrode material. Moreover, the π-conjugated NDI surface exhibited π–π stacking interactions with the GF surface, which favours fast charging and discharging between the electrode and electrolyte interface. Thus, all these factors provided good capacitance retention of the SC at a higher current density of about 4 A g^{-1}.

To further obtain insights into the electrochemical kinetics, the value of b at the reversible redox peaks (Fig. 3a) for **NDI-Trp-DP**/GF was estimated based on eqn (7)

$$I_p = av^b \quad (7)$$

(I = peak current response; v = scan rate (mV s^{-1})) through the linear fit of log(i) *versus* log(v) (Fig. 3b).[57] The estimated b value was found to be 0.99, demonstrating that the energy storage was dominated by the capacitive process based on redox-reactions of the **NDI-Trp-DP**/GF surface. The capacitive and diffusive current contributions to the total amount of current at

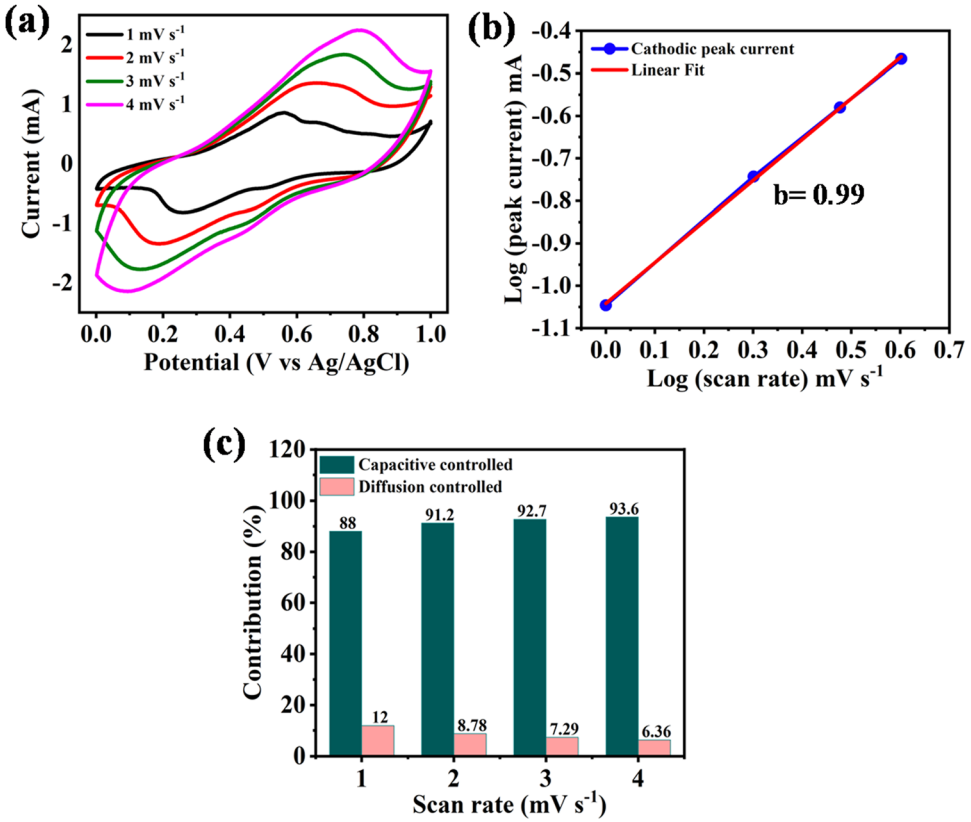

Fig. 3 (a) CV profiles of **NDI-Trp-DP**/GF recorded at various low scan rates. (b) The cathodic peak current (ip) with scan rate for **NDI-Trp-DP**/GF. (c) Relative contributions of the capacitive- and diffusion-controlled charge storage processes at different scan rates.

different scan rates were estimated by employing $k_1\nu$ and $k_2\nu^{1/2}$ in the equation $i = k_1\nu + k_2\nu^{1/2}$. The capacitive and diffusive current contributions for **NDI-Trp-DP**/GF at 1 to 4 mV s^{-1} are shown in Fig. 3c. The percentage capacitive-controlled contribution of **NDI-Trp-DP**/GF increased from 88% to 93.6% as we increased scan rate from 1 to 4 mV s^{-1}, while the percentage diffusion-controlled contribution of **NDI-Trp-DP**/GF decreased from 12% to 6.36% as we changed the scan rate from 1 to 4 mV s^{-1}. These results suggest that as the scan rate of the SC device increased, the capacitive-controlled contribution increased and the diffusive-controlled contribution obviously decreased (Fig. 3c).

Two-electrode symmetric supercapacitor (SSC)

To examine the practical applicability of **NDI-Trp-DP**/GF, the symmetric supercapacitor (SSC) device **NDI-Trp-DP**/GF//**NDI-Trp-DP**/GF was fabricated in a two-electrode (Swagelok) setup using 1 M H_2SO_4 as an electrolyte. Herein, **NDI-Trp-DP**/GF was utilized as the anode as well as the cathode electrode material. The electrochemical performance of **NDI-Trp-DP**/GF in the two-electrode SSC was examined using CV, GCD and electrochemical impedance spectroscopy (EIS), as shown in Fig. 4a, b, c and d, respectively. The CV curves of the as-fabricated SSC utilizing **NDI-Trp-DP**/GF were investigated to estimate the potential window at a 10 mV s^{-1} scan rate (Fig. S13a, ESI†). The CV study demonstrates that the potential windows reached a maximum at a 0 to 1.3 V potential window for the examined SSC. Moreover, the GCD measurements of **NDI-Trp-DP**/GF// **NDI-Trp-DP**/GF SSC at 1 A g^{-1} current density were carried out by employing various potential windows, *i.e.*, 0 to 0.8 V, 0 to 0.9 V, 0 to 1.0 V, 0 to 1.1 V, 0 to 1.2 V and 0 to 1.3 V (Fig. S13b, ESI†). To investigate the CV and GCD measurements by considering the aqueous electrolyte deposition, we selected 0 to 1.0 V potential windows for the examined SSC device. The CVs of the **NDI-Trp-DP**/GF//**NDI-Trp-DP**/GF SSC device configuration at scan rates of 5, 10, 15, 20, 25, 30 and 35 mV s^{-1} are shown in Fig. 4a. Fig. 4a indicated good electrochemical reversibility. At 5 mV s^{-1}, the **NDI-Trp-DP**/GF electrode in SSC device displayed a reversible redox peak indicating the pseudocapacitive behaviour of the device.[58] For the **NDI-Trp-DP**/GF// **NDI-Trp-DP**/GF SSC device, as the scan rate was increased from 5 to 35 mV s^{-1}, an increase in the area under the CV curves was observed. At higher scan rates, a rectangular shape along, with faradaic peaks, were found for the CV curves. These observations indicate that at higher scan rates, comparably slow redox reactions were happening due to higher internal resistance.[59] To calculate the C_{sp} of **NDI-Trp-DP**/GF//**NDI-Trp-DP**/GF, GCD tests were conducted to explore the advantages of **NDI-Trp-DP**/GF as an electrode material for the SSC device. The obtained GCD results of the **NDI-Trp-DP**/GF//**NDI-Trp-DP**/GF SSC device at a constant potential window of about 0 to 1.0 V at 0.5, 1, 2, 3, 4, 5 and 10 A g^{-1} are depicted in Fig. 4b. The distorted shape of the GCD curves suggests the pseudocapacitive nature of the SSC

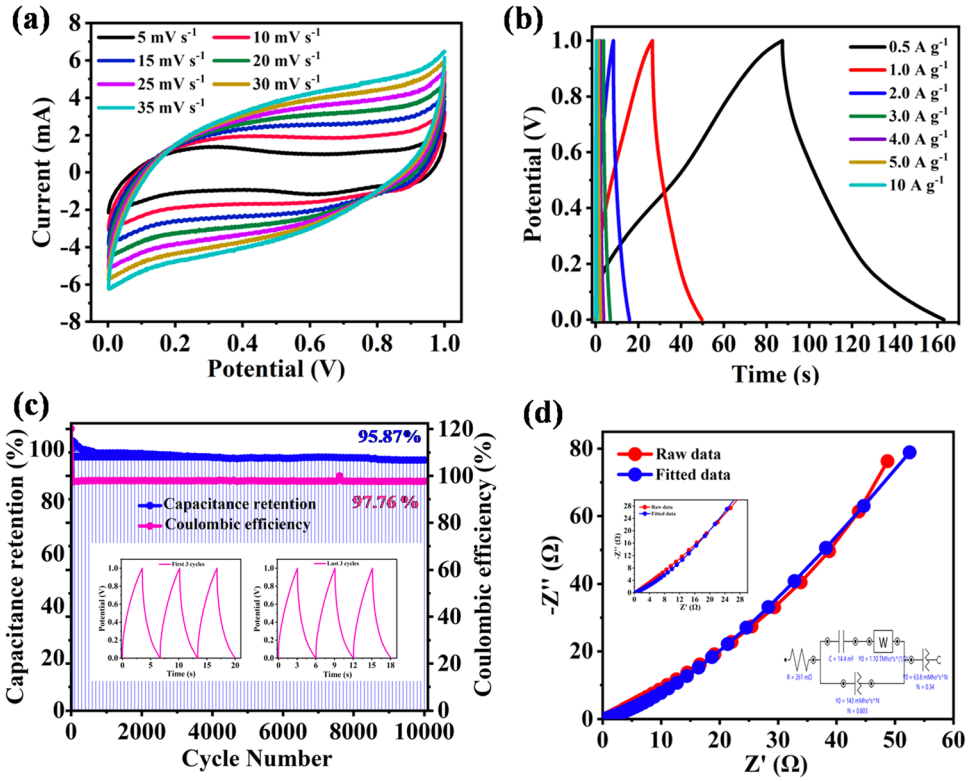

Fig. 4 Symmetric two electrode system: (a) CVs of the two-electrode system device at 5, 10, 15, 20, 25, 30, and 35 mV s^{-1}. (b) Two-electrode system GCD profiles at 0.5, 1, 2, 3, 4, 5, and 10 A g^{-1}. (c) Cycling stability from GCD studies at 3 A g^{-1}. (d) Nyquist plot at the open circuit potential examined in a two-electrode SSC; inset displays the electrical circuit used for data fitting.

device (Fig. 4b).[60] Moreover, ion diffusion was slower and enhanced the resistance in the SSC device. From the GCD curve at 0.5 A g^{-1} current density, the estimated C_{sp} using eqn (3) (Experimental Section) was found to be 152 F g^{-1} (Fig. 4b and Table 2). This is ascribed to the small IR drop at the 0.5 A g^{-1} current density, indicating the fast kinetics of the charge-storage process. The C_{sp} of the SSC calculated from the GCD curves indicated the excellent electrochemical properties of the device. The estimated C_{sp} for the two-electrode SSC system is higher than that of the reported organic electrode materials. Furthermore, as the current density increased from 0.5 A g^{-1} to 10 A g^{-1}, the C_{sp} of the **NDI-Trp-DP**/GF//**NDI-Trp-DP**/GF SSC device decreased gradually and reached C_{sp} = 10 F g^{-1} at 10 A g^{-1} (Fig. 4b, Table 2 and Fig. S14, ESI†). More impressively, the **NDI-Trp-DP**/GF-based SSC device shows a capacitance retention rate of about 6.5% at an ultrahigh current density of 10 A g^{-1}. This trend of decreasing C_{sp} at higher current density is found in organic-electrode-material-based SC devices. The decreased C_{sp} with increasing current density could be ascribed to the restricted ion migration and diffusion on the electrode surface.[61] The cycling stability of the **NDI-Trp-DP**/GF was examined by using GCD measurement. The cycling stability results for the **NDI-Trp-DP**/GF//**NDI-Trp-DP**/GF SSC device are displayed in Fig. 4c. After 10 000 GCD cycles, an ultrahigh C_{sp} retention of about 95.87% was found at 3 A g^{-1} current density, suggesting that the **NDI-Trp-DP**/GF electrode system be an ideal for real-world supercapacitor applications. This excellent

Table 2 Two-electrode system: C_{sp} from GCD studies at various current densities, specific energy, and specific power

GCD analysis			
Current density (A g^{-1})	Specific capacitance (F g^{-1})	Specific energy (W h kg^{-1})	Specific power (W kg^{-1})
0.5	152	19	900
1	92	11.50	1789.11
2	60.48	7.56	3600
3	38.56	4.82	5405.60
4	27.77	3.41	7071.43
5	21.60	2.70	9000
10	10.00	1.25	18 000

cycling stability of the **NDI-Trp-DP**/GF electrode should be due to the presence of the conjugated π-system on the graphene foil surface, which provides π–π stacking interactions. This non-covalent interaction between the organic material and the GF surface leads to the enhancement of surface contact area between the electrode and the electrolyte.[63]

Furthermore, for the **NDI-Trp-DP**/GF//**NDI-Trp-DP**/GF SSC device, the EIS data were analysed using Nyquist plots (Fig. 4d and Table 3). The experimental results data are well fitted by an electrical circuit (Fig. 4d, inset). R_s can obtained from the high-frequency region of the Nyquist plot, which is the combined internal resistance, the electrolyte ohmic resistance and the current collector intrinsic resistance. In the low-frequency region, the linearly vertical shape of the curve suggests fast

Table 3 EIS fitted parameters for NDI-Trp-DP/GF//NDI-Trp-DP/GF in SSC device

Parameter	R_s (Ω cm^2)	C_{dl} (mF)	C_{pe1} (F cm^2)	C_{pe2} (F cm^2)
NDI-Trp-DP/GF//**NDI-Trp-DP**/GF	0.261	14.4	0.340	0.803

diffusion of ions towards the electrode surface, enhancing the C_{sp} of the **NDI-Trp-DP**/GF.[64] The estimated value of R_s was found to be 0.261 Ω cm^2; this lower R_s value indicated that the **NDI-Trp-DP**/GF electrode material possesses good rate capability. The double-layer capacitance C_{dl} was calculated and found to be 14.4 mF. The calculated constant phase elements C_{pe1} and C_{pe2} equivalent to capacitance were observed to be 0.340 F cm^2 and 0.803 F cm^2. The lower C_{dl}, C_{pe1} and C_{pe2} values indicated that the electrode material exhibited very low EDCL behavior.

A Ragone plot for evaluating the energy and power densities of the as-fabricated **NDI-Trp-DP**/GF//**NDI-Trp-DP**/GF SSC device was created and is displayed in Fig. 5. The energy density and power density of the SSC device were estimated using eqn (4) and (5) (Experimental Section), respectively. The obtained results are tabulated in Table 2. As displayed in Fig. 5, the **NDI-Trp-DP**/GF//**NDI-Trp-DP**/GF SSC device exhibited an energy density of 19 W h kg^{-1} at a power density of 900 W kg^{-1} at 0.5 A g^{-1}. These were compared to the data for SCs reported in the literature, such as GH-DN//rGO-NDI,[34] NDI-2DP/CP//NDI-2DP/CP,[34] rGO-NDI-CN//rGO-NDI-CN,[35] NQ-DP/CP//NQDP/CP,[43] and P2P(NDI2ODOTh(NPV)//P2P(NDI2ODOTh(NPV).[62] Moreover, at 10 A g^{-1} (higher current density), the estimated energy and power densities are 1.25 W h kg^{-1} and 18 000 W kg^{-1}, respectively, which are comparable to those of SSC devices based on organic electrode materials. The high C_{sp} and higher energy density are attributed to the higher redox surface and demonstrate their promising potential for utilization in modern energy storage devices.

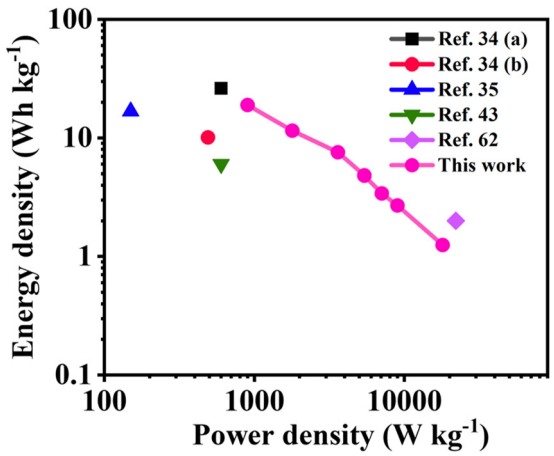

Fig. 5 Ragone plot comparing **NDI-Trp-DP**/GF//**NDI-Trp-DP**/GF with reported SCs: GH-DN//rGO-NDI,[34a] NDI-2DP/CP//NDI-2DP/CP,[34b] rGO-NDI-CN//rGO-NDI-CN,[35] NQ-DP/CP//NQ-DP/CP,[43] and P2P(NDI 2ODOTh(NPV)//P2P(NDI2ODOTh(NPV).[62]

Influence of different supercapacitor devices on C_{sp}

It is well documented that the estimated C_{sp} for an SC depends on the type of cell configuration.[65] We employed an **NDI-Trp-DP**/GF-based organic electrode material for the fabrication of a three-electrode supercapacitor device and a two-electrode symmetric SC, and the C_{sp} values were estimated using CV and GCD curves (Table 1, Fig. 2, and Table 2, Fig. 4, respectively). The calculated C_{sp} values for the three-electrode and symmetric two-electrode SC devices were 323 F g^{-1} and 152 F g^{-1} at a current density of 0.5 A g^{-1}. These results for the NDI-Pyr-DP/GF electrode in the two-electrode SSC cell set-up demonstrate the practical applicability of the material.

Physical and chemical electrode stability

The morphology and "external" structural physical stability of the as-prepared **NDI-Trp-DP**/GF were examined using FE-SEM. FE-SEM images of the **NDI-Trp-DP**/GF electrode material before and after the GCD performance test are depicted in Fig. 6a and b, respectively. The FE-SEM image of the electrode before GCD testing was found to show a 3D rough crystalline surface (Fig. 6a). The granular rough surface came from the organic materials in combination with the binder and GF. After 10000 GCD cycles, the morphology of the electrode was found to be unaltered (Fig. 6b). The FE-SEM results indicate that the as-fabricated electrode is physically stable after 10 000 GCD cycles. We presume that the physical stability of electrode could be responsible for the excellent cycling stability after 10 000 GCD cycles and retention of 95.87% C_{sp}.

Fig. 7a and b display the FT-IR spectra of the as-fabricated electrode before and after the GCD performance test. Before cycling, the electrode material exhibited IR peaks at 3428, 2929, 1640, 1337, 1230, 743 and 536 cm^{-1}. As shown in Fig. 7b, after 10 000 GCD cycles, the characteristic peaks appeared at 3418, 2925, 1645, 1356, 1160, 757 and 537 cm^{-1}. These results indicate that **NDI-Trp-DP**/GF can be tightly coated on the GF surface, which leads to chemical stability even after 10 000 GCD

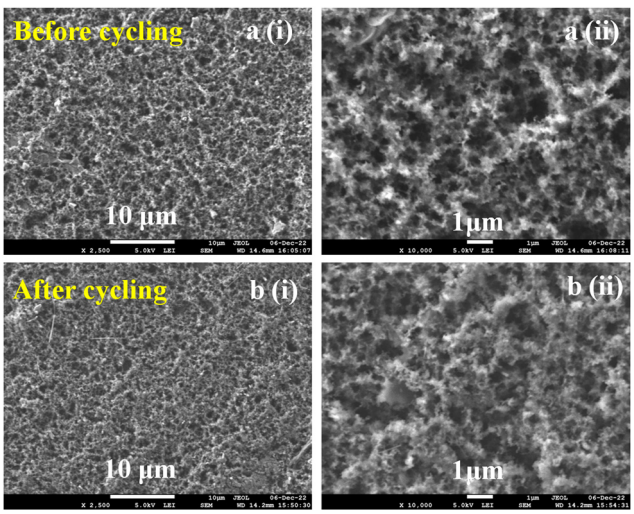

Fig. 6 SEM images of the **NDI-Trp-DP**/GF electrode (a) (i–ii) before and (b) (i–ii) after the cyclic stability test.

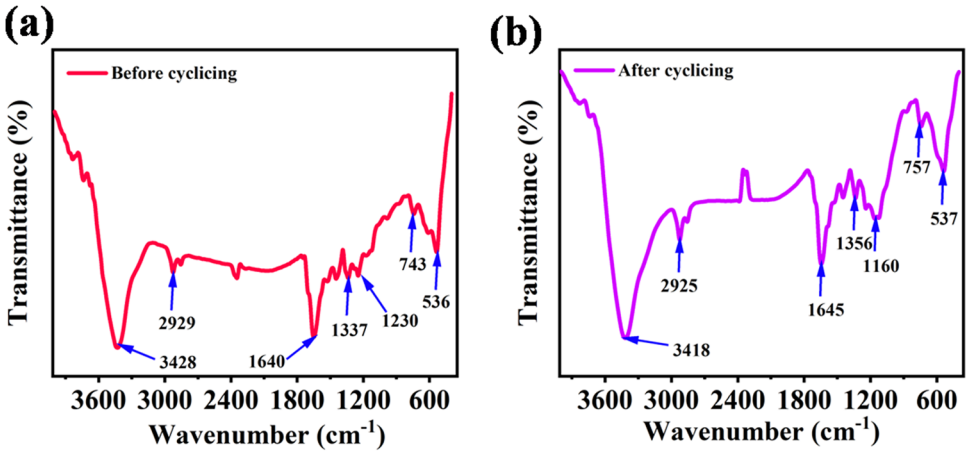

Fig. 7 FT-IR spectra of **NDI-Trp-DP**/GF electrode: (a) before and (b) after cyclic stability testing.

cycles. Thus, the mechanical and chemical stability of the **NDI-Trp-DP**/GF electrode during charging and discharging resulted in prolonged cycling stability of the SSC cell architecture. These features of the **NDI-Trp-DP**/GF electrode seem suitable for its utilization in technological development.

The electrochemical properties of the three-electrode SC system and two-electrode SSC device architecture fabricated utilizing the **NDI-Trp-DP**/GF organic electrode material indicate promise for energy storage applications. Moreover, the excellent cycling stability, high energy density and power density associated with the **NDI-Trp-DP**/GF electrode in the two-electrode SSC device make it a promising material for large-scale energy storage devices for electrical vehicles and flexible electronics applications.

Working mechanism of NDI-Trp-DP

The redox reaction mechanism of **NDI-Trp-DP** system is presented in Fig. 8. We presume that in presence of aqueous H_2SO_4 electrolyte, the reaction occurs in two steps: in the first step, the NDI imide carbonyl functional groups are protonated, yielding $[NDI]^{\bullet -}{\cdot}H^+$, and in the second step, incorporation of another H^+ into the imide carbonyl of the NDI ring system results in $[NDI]^{\bullet -}{\cdot}2H^+$.[32–34] Furthermore, the redox chemistry of tryptophan[37–40] as well as dopamine[41–46] with a two-electron transfer process are involved. Thus, one NDI ring system, two tryptophan and two dopamine molecular subunits participated, resulting in a ten-electron/proton reversible redox reaction process (Fig. 8).[66–69]

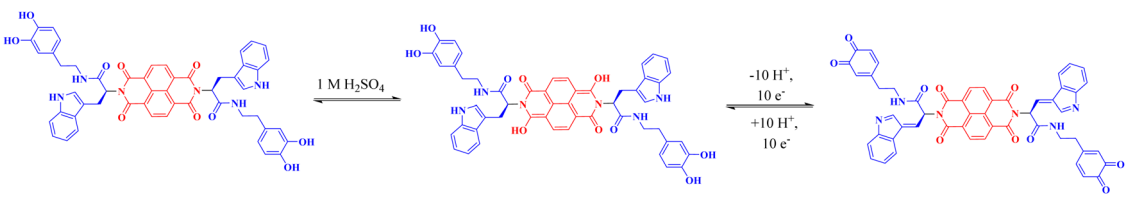

Fig. 8 Schematic of the plausible proposed reversible redox mechanism of the **NDI-Trp-DP** molecular architecture.

Table 4 Comparison of the electrochemical performance of **NDI-Trp-DP**/GF//**NDI-Trp-DP**/GF symmetric supercapacitor devices with those of organic materials reported in the literature

Sr. No	Electrode material	Electrolyte	Voltage (V)	Current density (A g^{-1})	C_{sp} GCD (F g^{-1})	Energy density (W h kg^{-1})	Power density (W kg^{-1})	No. cycles @ current density (A g^{-1})	C_{sp} Retention (%)	Ref No.
1	P2P(NDI2ODOThCNPV)// P2P(NDI2ODOThCNPV)	0.5 M H_2SO_4	−0.7 to 0.5	0.5	124	2.0	22000	5000 @ 5	100[a]	62
2	BQ-DP//BQ-DP	1 M H_2SO_4	0 to 1	9.5	416	13.88	22000	5000 @ 9.5	70.6[a]	46
3	NDI-2DP/CP//NDI-2DP/CP	1 M H_2SO_4	0 to 1	0.5	73.1	10.1	490	4000 @ 3	97[a]	34*b*
4	NQ-DP/CP//NQ-DP/CP	1 M H_2SO_4	0 to 1.2	0.5	43.4	6.00	600	5000 @ 4	92[a]	43
5	GH-DN//rGO-NDI	1 M H_2SO_4	0 to 1.6	1	111.3	26.3	600	8000 @ 3	83.4[b]	34*b*
6	PDI-Py/GF//PDI-Py/GF	1 M H_2SO_4	−0.2 to 1.5	1	128	46	3060	10 000 @ 5	95[a]	63
7	rGO/NDI-CN//rGO/NDI-CN	1 M H_2SO_4	0 to 1.2	0.5	336	16.80	149.60	10 000 @ 10	80[c]	35
8	**NDI-Trp-DP**/GF//**NDI-Trp**/GF	1 M H_2SO_4	0 to 1	0.5	152	19	900	10 000 @ 3	95.87[a]	Present work

[a] Symmetric two-electrode system. [b] Asymmetric two-electrode system. [c] Three-electrode system.

The results for the SSC based on the **NDI-Trp-DP**/GF//**NDI-Trp-DP**/GF electrode material will bring about advanced organic supercapacitors with higher energy density, long-term cycling stability and rate capability. Moreover, optimizing the redox behaviour of the organic electrode material can enhance the capacitance of the SC cells (Table 4).

Conclusions

The supercapacitor applications of **NDI-Trp-DP**-deposited graphite foil electrodes have been shown using aqueous 1 M H_2SO_4 electrolyte. The three-electrode SC device based on the NDI-the Trp-DP/GF electrode material showed a maximum C_{sp} of 267.90 F g^{-1} at 5 mV s^{-1} and 323 F g^{-1} at 0.5 A g^{-1} as examined using CV and GCD measurements vs Ag/AgCl in 1 M H_2SO_4 electrolyte, respectively. Moreover, the two-electrode symmetric SC device fabricated using **NDI-Trp-DP**/GF electrodes in 1 M H_2SO_4 exhibited an excellent C_{sp} of 152 F g^{-1} at 0.5 A g^{-1}. At 0.5 A g^{-1}, the SSC device displayed a high energy density of 19 W h kg^{-1} at a power density of 900 W kg^{-1}. The **NDI-Trp-DP**/GF electrode exhibits an excellent cycling stability of about 95.87% after 10 000 galvanostatic charging–discharging (GCD) cycles, and 97.76% continuous GCD charge–discharge cycle coulombic efficiency. The high performance of the **NDI-Trp-DP**/GF electrode material is attributed to the number of redox subunits in the molecular architecture and the chemical and physical stability of the electrode. The high performance of **NDI-Trp-DP**-based organic material is promising for its viable SC application. Thus, the use of organic materials from rich renewable sources with high performance in SCs will significantly reduce the cost of SC devices for real-world applications.

Data availability statement

Experimental data is available with reasonable request to the corresponding authors.

Author contributions

Sudhir D. Jagdale: methodology, synthesis and characterization, device fabrication and measurement; Chepuri R. K. Rao: methodology, writing – review & editing; Sidhanath V. Bhosale: conceptualization, supervision, funding acquisition, writing – original draft, review & editing, investigation; Sheshanath V. Bhosale: conceptualization, resources, writing – review & editing.

Conflicts of interest

The authors declare no competing financial interest.

Acknowledgements

Sidhanath Vishwanath Bhosale (IICT) is grateful for financial support from BRNS under the project No.: 58/14/01/2020-BRNS/37047 and the Director, CSIR-IICT (MS No. IICT/Pubs./2023/066). Sheshanath Vishwanath Bhosale (GU) acknowledges University Grant Commission (UGC) Faculty Research Program, New Delhi, India (F.4-5(50-FRP) (IV-Cycle)/2017(BSR)) for an award of Professorship and also acknowledges Council of Scientific & Industrial Research (*CSIR*), India for providing support, code No. 02(0357)/19/EMR-II. Sudhir D. Jagdale is grateful for financial support through SRF from UGC, New Delhi.

Notes and references

1 O. Ellabban, H. Abu-Rub and F. Blaabjerg, *Renewable Sustainable Energy Rev.*, 2014, **39**, 748–764.
2 N. Armaroli and V. Balzani, *Energy Environ. Sci.*, 2011, **4**, 3193–3222.
3 (*a*) W.-J. Liu, H. Jiang and H.-Q. Yu, *Energy Environ. Sci.*, 2019, **12**, 1751–1779; (*b*) T. Liu, L. Zhang, B. Chemg and J. Yu, *Adv. Energy Mater.*, 2019, **9**, 1803900; (*c*) H. Jin, J. Li, Y. Yuan, J. Wang, J. Lu and S. Wang, *Adv. Energy Mater.*, 2018, **8**, 1801007.
4 L. Yangyang, Y. Chenhui, T. Yapeng, T. Yi, Y. Xingtian and Q. J. Wenxiu, *J. Power Sources*, 2020, **450**, 227694.
5 R. Bondade, Y. Zhang, B. Wei, T. Gu, H. Chen and D. Ma, *IEEE Trans. Ind. Electron.*, 2016, **63**, 2850–2861.
6 S. Liu, L. Kang, J. Zhang, C. S. Jun and Y. Yamauchi, *ACS Energy Lett.*, 2021, **6**, 4127–4154.
7 W.-H. Li, W.-H. Deng, G.-E. Wang and G. Xu, *Energy Chem.*, 2020, **2**, 100029.
8 M. Beidaghi and Y. Gogotsi, *Energy Environ. Sci.*, 2014, **7**, 867–884.
9 P. Simon and Y. Gogotsi, *Nat. Mater.*, 2008, **7**, 845–854.
10 N. Kamboj, T. Purkait, M. Das, S. Sarkar, K. S. Hazra and R. S. Dey, *Energy Environ. Sci.*, 2019, **12**, 2507.
11 J. Zhang, N. Kong, S. Uzun, A. Levitt, S. Seyedin, P. A. Lynch, S. Qin, M. Han, W. Yang, J. Liu, X. Wang, Y. Gogotsi and J. M. Razal, *Adv. Mater.*, 2020, **32**, 2001093.
12 G. Yury, *Nature*, 2014, **509**, 568–569.
13 P. K. Sharma, A. Arora and S. K. Tripathi, *J. Energy Storage*, 2019, **21**, 801–825.
14 A. González, E. Goikolea, J. A. Barrena and R. Mysyk, *Renewable Sustainable Energy Rev.*, 2016, **58**, 1189–1206.
15 L. G. Beka, X. Li, X. Wang, C. Han and W. Liu, *RSC Adv.*, 2019, **9**, 26637–26645.
16 P. Veerakumar, A. Sangili, S. Manavalan, P. Thanasekaran and K.-C. Lin, *Ind. Eng. Chem. Res.*, 2020, **59**, 6347–6374.
17 D. Majumdar, T. Maiyalagan and Z. Jiang, *ChemElectroChem*, 2019, **6**, 4343–4372.
18 S. Korkmaz, F. Meydaneri Tezel and İ. A. Kariper, *J. Alloys Compd.*, 2018, **754**, 14–25.
19 A. Eftekhari, L. Li and Y. Yang, *J. Power Sources*, 2017, **347**, 86–107.
20 R. B. Choudhary, S. Ansari and B. Purty, *J. Energy Storage*, 2020, **29**, 101302.
21 (*a*) J. R. Miller and P. Simon, *Science*, 2008, **321**, 651–652; (*b*) L. Wang, T. Wu, S. Du, M. Pei, W. Guo and S. Wei, *RSC Adv.*, 2016, **6**, 1004–1011.

22 T. B. Schon, B. T. McAllister, P. F. Li and D. S. Seferos, *Chem. Soc. Rev.*, 2016, **45**, 6345–6404.
23 M. Boota, C. Chen, M. Bécuwe, L. Miao and Y. Gogotsi, *Energy Environ. Sci.*, 2016, **9**, 2586–2594.
24 J. Yang, P. Xiong, Y. Shi, P. Sun, Z. Wang, Z. Chen and Y. Xu, *Adv. Funct. Mater.*, 2020, **30**, 1909597.
25 R. Shi, C. Han, H. Duan, L. Xu, D. Zhou, H. Li, J. Li, F. Kang, B. Li and G. Wang, *Adv. Energy Mater.*, 2018, **8**, 1802088.
26 S. K. Kim, J. Cho, J. S. Moore, H. S. Park and P. V. Braun, *Adv. Funct. Mater.*, 2016, **26**, 903–910.
27 P. Poizot, J. Gaubiher, S. Renault, L. Duois, Y. Liang and Y. Yao, *Chem. Rev.*, 2020, **120**, 6490–6557.
28 S. P. Ega and P. Srinivasan, *J. Energy Storage*, 2022, **47**, 103700.
29 M. R. Biradar, S. V. Bhosale, P. P. Morajkar and S. V. Bhosale, *Fuel*, 2022, **310**, 122487.
30 A. M. Bryan, L. M. Lu, Y. Santino, S. Acharya and J. M. D'Arcy, *Chem. Mater.*, 2016, **28**, 5989–5998.
31 A. D. Adhikari, A. Morag, J. Seo, J. M. Kim and R. Jelinek, *ChemSusChem*, 2020, **13**, 3230–3236.
32 M. A. Kobaisi, S. V. Bhosale., K. Latham, A. M. Raynor and S. V. Bhosale, *Chem. Rev.*, 2016, **116**, 11685–11796.
33 S. V. Bhosale, M. A. Kobaisi, R. W. Jadhav, P. P. Morajkar, L. A. Jones and S. George, *Chem. Soc. Rev.*, 2021, **50**, 9845–9998.
34 (*a*) F. Ma, Z. Hu, L. Jiao, X. Wang, Y. Yang, Z. Li and Y. He, *Adv. Mater. Interfaces*, 2021, **8**, 2002161; (*b*) M. R. Biradar, A. V. Salkar, P. P. Morajkar, S. V. Bhosale and S. V. Bhosale, *New J. Chem.*, 2021, **45**, 9346–9357; (*c*) C. Weng, X. Li, Z. Yang, H. Long, C. Lu, L. Dong, S. Zhao and L. A. Tan, *Chem. Commun.*, 2022, **58**, 6809–6812.
35 A. B. Deshmukh, M. R. Biradar, M. D. Pawar, S. V. Bhosale and M. V. Shelke, *J. Energy Storage*, 2022, **56**, 106036.
36 J. C. Ma and D. A. Dougherty, *Chem. Rev.*, 1997, **97**, 1303–1324.
37 C. R. Hoopes, F. J. Garcia, A. M. Sarkar, N. J. Kuehl, D. T. Barkan, N. L. Collins, G. E. Meister, T. R. Bramhall, C.-H. Hsu, M. D. Jones, M. Schirle and M. T. Taylor, *J. Am. Chem. Soc.*, 2022, **144**, 6227–6236.
38 H. Wang, Y. Yang, X. Zhou, R. Li and Z. Li, *New J. Chem.*, 2017, **41**, 1110–1118.
39 R. Srinivasan, E. Elaiyappillai, S. Gowri, A. Bella, A. B. Sathiyan and J. P. Meenatchia Merlin, *Phys. Chem. Chem. Phys.*, 2019, **21**, 11829–11838.
40 L. Ruiyi, H. Keyang, Y. Yongqiang, Z. Haiyan and L. Zaijun, *Chem. Eng. J.*, 2021, **426**, 130893.
41 A. Björklund and S. B. Dunnett, *Trends Neurosci.*, 2007, **30**, 194–202.
42 G. Wang, X. Huang and P. Jiang, *Sci. Rep.*, 2017, **7**, 43071.
43 M. R. Biradar, A. V. Salkar, P. P. Morajkar, S. V. Bhosale and S. V. Bhosale, *New J. Chem.*, 2021, **45**, 5154–5164.
44 V. Veeramani, R. Madhu, S.-M. Chen and M. Sivakumar, *ACS Sustainable Chem. Eng.*, 2016, **4**, 5013–5020.
45 P. Flouda, S. A. Shah, D. C. Lagoudas, M. J. Green and J. L. Lutkenhaus, *Matter*, 2019, **1**, 1532–1546.
46 S. P. Ega, M. R. Biradar, P. Srinivasan and S. V. Bhosale, *Electrochim. Acta*, 2020, **357**, 136835.
47 S. P. Goskulwad, V. G. More, D. D. La, R. S. Bhosale, A. L. Puyad, S. V. Bhosale and S. V. Bhosale, *Ind. J. Chem.*, 2019, **58B**, 200–208.
48 (*a*) W. Liyanage, P. W. Rubeo and B. L. Nilsson, *Interface Focus*, 2017, **7**, 20160099; (*b*) C. Wiberg, F. Owusu, E. Wang and E. Ahlberg, *Energy Technol.*, 2019, **7**, 1900843; (*c*) C. Liu, J. Wang, J. Li, R. Luo, J. Shen, X. Sun, W. Han and L. Wang, *ACS Appl. Mater. Interfaces*, 2015, **7**, 18609–18617; (*d*) S. D. Jagdale, C. R. K. Rao, S. V. Bhosale and S. V. Bhosale, *J. Energy Storage.*, 2023, **66**, 107482.
49 (*a*) J. Yu, N. Fu, J. Zhao, R. Liu, F. Li, Y. Du and Z. Yang, *ACS Omega*, 2019, **4**, 15904–15911; (*b*) R. Velayuthama, R. Manikandana, J. Raj, A. M. Kale, C. Kaya, K. Palanisamye and B. C. Kim, *J. Alloys Compd.*, 2021, **863**, 158332.
50 A. M. Kale, R. Manikandan, C. J. Raj, R. Velayutham, W.-J. Cho and B. C. Kim, *Appl. Surf. Sci.*, 2021, **542**, 148716.
51 A. Sangili, V. Vinothkumar, S.-M. Chen, P. Veerakumar, C.-W. Chang, I. P. Muthuselvam and K.-C. Lin, *J. Phys. Chem. C*, 2020, **124**, 25821–25834.
52 J. Yan, Z. Fan, W. Sun, G. Ning, T. Wei, Q. Zhang, R. Zhang, L. Zhi and F. Wei, *Adv. Funct. Mater.*, 2012, **22**, 2632–2641.
53 B. Huskinson, M. P. Marshak, C. Suh, S. Er, M. R. Gerhardt, C. J. Galvin and M. J. Aziz, *Nature*, 2014, **505**, 195–198.
54 D. D. Potphode, L. Sinha and P. M. Shirage, *Appl. Surf. Sci.*, 2019, **469**, 162–172.
55 K. K. Ramakrihnan, C. Nithya and R. Karvmbu, *Nanoscale Adv.*, 2019, **1**, 334–341.
56 C. Molji, A. S. Aashish, K. Neethu and S. J. Devaki, *J. Mater. Chem. A*, 2017, **5**, 16636–16645.
57 H. Lindstrom, S. Sodergren, A. Solbrand, H. Rensmo, J. Hjelm, A. Hagfeldt and S. E. Lindquist, *J. Phys. Chem. B*, 1997, **101**, 7717–7722.
58 J. Wang, J. Polleux, J. Lim and B. Dunn, *J. Phys. Chem. C*, 2007, **111**, 14925–14931.
59 Y. Jiang and J. Liu, *Energy Environ. Mater.*, 2019, **2**, 30–37.
60 B. Pal, S. Yang, S. Ramesh, V. Thangadurai and R. Jose, *Nanoscale Adv.*, 2019, **1**, 3807–3835.
61 H. Ma, H. Chen, Y. Hu, B. Yang, J. Feng, Y. Xu, Y. Sun, H. Cheng, C. Li, X. Yan and L. Qu, *Energy Environ. Sci.*, 2022, **15**, 1131–1143.
62 S. Sharma, R. Soni, S. Kurugot and S. K. Asha, *Macromolecules*, 2018, **51**, 954–965.
63 J. C. Rusell, V. A. Posey, J. Gray, R. May, D. A. Reed, H. Zhang, L. E. Marbella, M. L. Steigerwald, Y. Yang, X. Roy, C. Nuckolls and S. R. Peurifoy, *Nat. Mater.*, 2021, **20**, 1136–1141.
64 B. K. Kim, S. Sy, A. Yu and J. Zhang, *Electrochemical Supercapacitors for Energy Storage and Conversion*, Wiley-VCH, 2015.
65 M. R. Biradar, A. M. Kale, B. C. Kim, S. V. Bhosale and S. V. Bhosale, *Energy Technol.*, 2022, **10**, 2200154.
66 V. S. Sapner, P. P. Chavan, R. V. Digraskar, S. S. Narwade, B. B. Mulik, S. M. Mali and B. R. Sathe, *ChemElectroChem*, 2018, **5**, 3191–3197.
67 B. Song, J. Zhao, M. Wang, J. Mullavey, Y. Zhu, Z. Geng, D. Chen, Y. Ding, K.-S. Moon, M. Liu and C.-P. Wong, *Nano Energy*, 2017, **31**, 183–193.
68 M. A. Azam, M. A. Azizan, N. S. A. Manaf, R. Izamshah and N. Mohamad, *Adv. Sci. Eng. Med.*, 2014, **6**, 1–4.
69 H. Li, J. Wang, Q. Chub, Z. Wang, F. Zhanga and S. Wang, *J. Power Sources*, 2009, **190**, 578–586.